UAS-Based Tools for Mapping and Monitoring Hydrothermal Systems: An Example from Mammoth Lakes, California

Laurie A. Zielinski[1], Jonathan M. Glen[1], Tait E. Earney[1], Grant H. Rea-Downing[2,1], R. Greg Vaughan[3], Peter J. Kelly[4], Gordon H. Keller[5,1], Branden J. Dean[1], William D. Schermerhorn[6]

1. **U.S. Geological Survey, Geology, Minerals, Energy, and Geophysics Science Center, Moffett Field, CA**

2. **University of Utah, Department of Geology and Geophysics, Salt Lake City, UT**

3. **U.S. Geological Survey, Astrogeology Science Center, Flagstaff, AZ**

4. **U.S. Geological Survey, Volcano Hazards Program, Vancouver, WA**

5. **University of California, Santa Cruz, Department of Electrical and Computer Engineering, Santa Cruz, CA**

6. **Mount Vernon, WA**

Keywords

Unoccupied Aerial Systems (UAS), Hydrothermal Monitoring, Long Valley Caldera, Thermal Infrared (TIR), Magnetics, Multi-GAS, Photogrammetry, Gravity

ABSTRACT

Unoccupied aerial systems (UAS) can accommodate a variety of tools for mapping and monitoring hydrothermal systems (e.g., magnetic, gas, photogrammetry, and thermal infrared [TIR]). These platforms offer increased speed, coverage area, and uniformity compared to ground-based measurements, as well as lower flight height – and therefore higher resolution – than occupied aircraft.

We adapted a suite of tools for use with UAS and implemented these methods in a study focused on the area around Shady Rest Park, Mammoth Lakes, California, within the Long Valley Caldera. This location, which contains tree kills, gas vents, soil gas emissions, heated ground, and hydrothermal alteration, is the site of ongoing efforts to monitor changes in the surface expression of the local hydrothermal system. The methods applied in this study included: (1)

airborne visible imagery for surficial mapping and the creation of high-resolution digital elevation models; (2) airborne magnetic measurements; (3) airborne TIR imagery; (4) airborne gas emission measurements; and (5) ground-based gravity measurements.

We conducted these surveys in May and October of 2021, in part to establish baseline TIR and gas data against which future changes to the hydrothermal system may be assessed. UAS-based magnetic and ground-based gravity data were collected to map subsurface geology and to characterize potential subsurface controls on thermal anomalies and gas emissions.

Results of these efforts at mapping and monitoring the hydrothermal system at Mammoth Lakes demonstrate how an integrated UAS- and ground-based approach may be applied more broadly to study other known or potential hydrothermal and volcanic systems. We consider the benefits and limitations of each method, particularly the TIR and gas sensors, which have less well-developed processing techniques in place for UAS applications. By integrating results from several of these different methods, however, the limitations facing each individual approach may be mitigated, and a better understanding of the hydrothermal system may be reached.

1. Introduction

Unoccupied aerial systems (UAS) are increasingly recognized as efficient platforms for hosting various scientific measurement tools. Compared to ground-based investigations, UAS offer numerous advantages for mapping and monitoring hydrothermal systems. For instance, UAS afford increased speed, and therefore allow larger areas to be covered with uniform measurements. Airborne surveys also permit data collection at remote sites with limited ground access and offer greater safety for researchers, particularly in active hydrothermal areas with abundant gas vents, hot springs, or fragile hydrothermal mineral deposits. Occupied aircraft have the same advantages but generally require greater flight altitudes that result in slightly lower resolution data, although they can cover a larger area in a single mission. Contracting an occupied aircraft is also significantly more expensive than a UAS and can pose a safety risk for aircraft operators. Additionally, the surveys performed using contracted occupied aircraft must be planned in advance and cannot be adjusted during data acquisition. Adapting geoscientific tools for use with UAS can mitigate the limitations of ground-based investigations of geothermal systems, while maintaining very high resolution and requiring lower costs over the long term.

Numerous potential applications of UAS to the mapping and monitoring of hydrothermal systems include structure from motion (SfM) photogrammetry, magnetics, thermal infrared (TIR) imagery, and gas emissions measurements. UAS-borne applications of magnetics and SfM have been employed for geoscientific purposes for years, because operational procedures and processing steps were relatively straightforward to carry over from practices developed for occupied aircraft (e.g., Kaub et al., 2020; Kaub et al., 2021; Chesley et al., 2017; Jackisch et al., 2020; Walter et al., 2020; Parvar et al., 2017; De Smet et al., 2021). While UAS have been used to capture TIR imagery of geothermal areas, the underlying sensor technology and corresponding best practices remain under development (Präg et al., 2020; Harvey et al., 2016; Nishar et al., 2016; Chio and Lin, 2017). Known challenges of deploying thermal cameras on UAS include variable wind speeds during flight and the impracticality of mounting cooled thermal cameras (which are typically larger and heavier) on UAS, meaning that uncooled thermal cameras must be used. These uncooled sensors are associated with temperature calibration drift and vignetting (reduction in brightness near image edges), all of which cannot be entirely compensated by

cameras' internal calibration (Kelly et al., 2019). Likewise, UAS-borne gas emissions measurements have been performed at active volcanoes (Liu et al., 2019; Stix et al., 2018; Müller et al., 2021), but applications remain limited, in part due to the large effect of wind, particularly in areas with lower gas concentrations.

We tested several of these applications of UAS at the site of Shady Rest, in Mammoth Lakes, California, located in the Long Valley Caldera (Figure 1). The present Long Valley Caldera was formed 760,000 years ago by the eruption of the Bishop Tuff (Bailey et al., 1976). Subsequent rhyolitic intracaldera volcanism has resulted in magmatic uplift and the formation of a resurgent dome. The geologic units exposed in the area are largely Quaternary volcanics and glacial deposits (Figure 2; Hildreth and Fierstein, 2016). Long Valley Caldera has been studied as a key geothermal site for decades due to an increase in earthquakes and gas emissions (Bailey et al., 1976), and the nearby Casa Diablo power plant began production in 1985 (Sorey et al., 1995). The area around Mammoth Lakes is characterized by active gas emissions and has been the site of numerous temporal gas measurements (e.g., Sorey et al., 1998; Lewicki, 2021).

Shady Rest was selected as our test site due to the multiple surface expressions of the underlying hydrothermal system, including tree kills from carbon dioxide (CO_2), gas vents, heated ground, and hydrothermal alteration. Previous ground-based studies at Shady Rest show a positive correlation between soil temperatures and diffuse CO_2 flux, with increases in the areal extent of heated ground and in hydrogen sulfide (H_2S) concentrations in recent years (Bergfeld and Evans, 2011; Bergfeld et al., 2015). In 2016, baseline TIR data were also collected in a large survey over the geothermal area using an occupied fixed-wing Cessna aircraft at a height of 1,800 m above ground level, with a spatial resolution of ~0.9 m (Vaughan et al., 2018).

During two field sessions in May and October 2021, we used two UAS to collect four datasets: SfM, magnetics, TIR, and Multi-GAS, as well as a complementary ground-based gravity dataset. The visible SfM data enable the creation of high-resolution orthomosaics and digital elevation models (DEMs), which assist with flight planning and interpretation. Magnetic and gravity data aid in mapping subsurface geology and other controls on the hydrothermal system, while TIR and gas data aid in characterizing areas of thermal activity. This study is a step towards assessing the utility of these tools, and we consider how they might be applied more broadly for mapping and monitoring other hydrothermal systems. We also begin to establish baseline measurements to compare with data from any future collection efforts as part of the larger program to monitor temporal variations in the hydrothermal system at Mammoth Lakes.

2. Structure from Motion

To generate high-resolution photo orthomosaics and DEMs using photogrammetry, visible imagery was collected with a Zenmuse X3 camera mounted on a DJI Matrice 100 UAS platform (Figure 3A; DJI Technology Company Ltd.). Flights were flown at a speed of 12 m/s at a height of 120 m above terrain. The camera was oriented downward, side and forward overlap were ~60%, and camera triggers were every 3 s, for a ground resolution of 5 cm. The shutter speed was set to 1/2,500 s and the ISO (light sensitivity) to 200. For geometric control, five ground control points were deployed and measured with a Trimble Geo 7X differential global positioning system (GPS; Trimble, Inc.), which has a post-processing vertical and horizontal precision of <5 cm. The images were processed in Agisoft Metashape to construct a 5 cm/pixel orthomosaic and a 20 cm/pixel DEM, which provide high-resolution data useful for comparing

with complementary UAS- and ground-based datasets and for planning flights around potential obstacles.

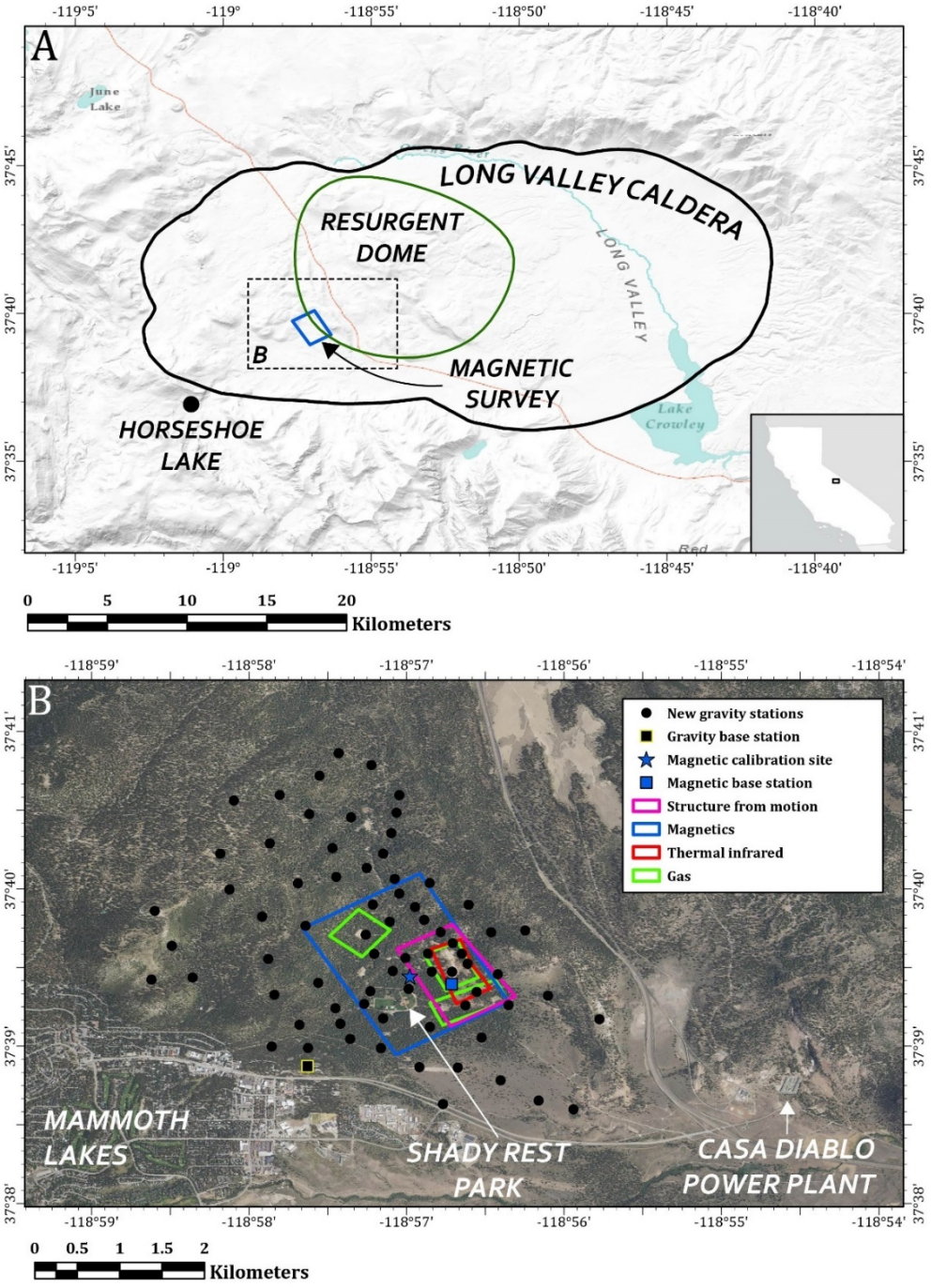

Figure 1: Index maps of study site. (A) Shaded-relief topographic map showing location of study area within the Long Valley Caldera, with dashed box showing extent of (B). Green line denotes extent of resurgent dome. Base map is USGS Shaded Relief from The National Map. Caldera and resurgent dome boundaries modified after Bailey (1989). (B) Extents of data collected in and around Shady Rest Park, in the town of Mammoth Lakes, California, near the Casa Diablo geothermal power plant. Imagery acquired by the U.S. Department of Agriculture as part of the National Agriculture Imagery Program (NAIP), accessed through ArcGIS Online.

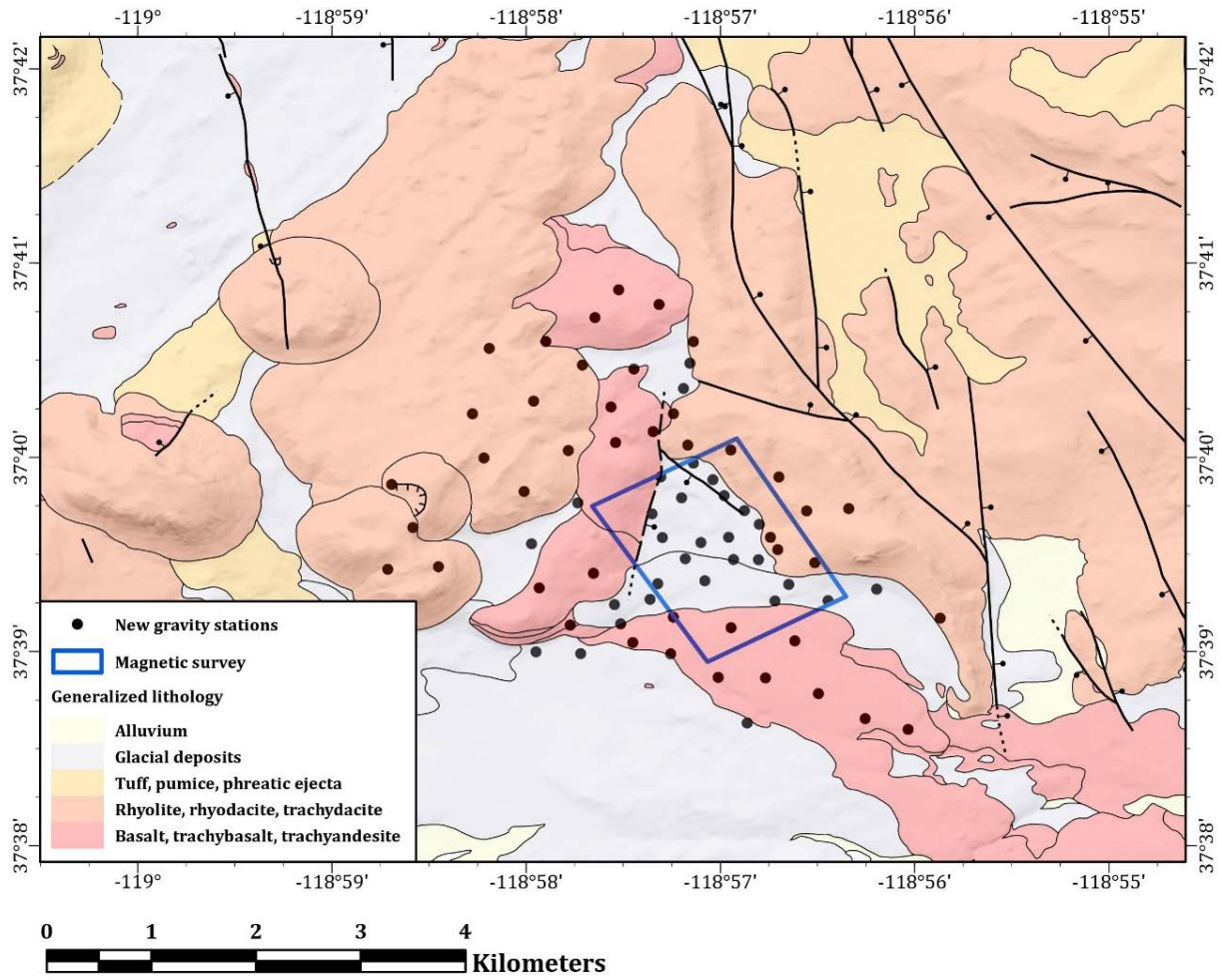

Figure 2: Generalized geologic map of the study area, modified after Robinson et al. (2016), overlain on shaded-relief map and showing newly collected gravity data and extent of the UAS-borne magnetic survey. Normal faults are shown with symbol on down-dropped side. Same extent as Figures 9 and 10.

The orthomosaic and DEM (Figure 4) produced from the SfM data provide accurate and high-resolution imagery and surface elevation data for the main study area (Figure 1). There are minor artefacts in the SfM data, including slight NNW-trending features in the orthomosaic, associated with variable lighting conditions across flight lines, and pits in the DEM, associated with vegetation. These data are useful for discerning hydrothermal features such as the tree kill area and the fumarole mound, and for establishing a baseline for any ground deformation associated with changes to the hydrothermal system. The DEM and SfM data also played an invaluable role in planning flights for the complementary datasets: having a high-resolution DEM is imperative to planning automated UAS-borne gas and magnetic surveys, due to the necessity of low flight heights and the extensive tree coverage in the area.

Figure 3: Photos of UAS platforms with payloads circled. (A) DJI Matrice 100 with Zenmuse X3 camera. Drone is 65-cm diameter. (B) DJI Matrice 600 Pro with Sensys MagDrone R3 magnetometer on carbon fiber frame. Drone is ~1.6-m diameter. (C) DJI Matrice 600 Pro with FLIR Duo Pro R thermal camera, mounted on a Gremsy S1 V3 gimbal. (D) DJI Matrice 600 Pro with U.S. Geological Survey UAS Multi-GAS instrument. Photographs by Jonathan Glen, U.S. Geological Survey.

3. Magnetics

For the airborne magnetometry survey, a Sensys MagDrone R3 was mounted on a rigid carbon fiber frame 0.5 m below a DJI Matrice 600 Pro UAS platform (Kaub et al., 2020; Figure 3B). This vector magnetometer system is designed for UAS and features two three-axis fluxgate magnetometers and a GPS receiver. Surveys were flown at 10 m/s at 60 m above terrain. Flight lines were oriented ENE/WSW, with 60 m spacing between them. Perpendicular tie lines with 150 m spacing were also flown to allow for tie line levelling (Figure 5A).

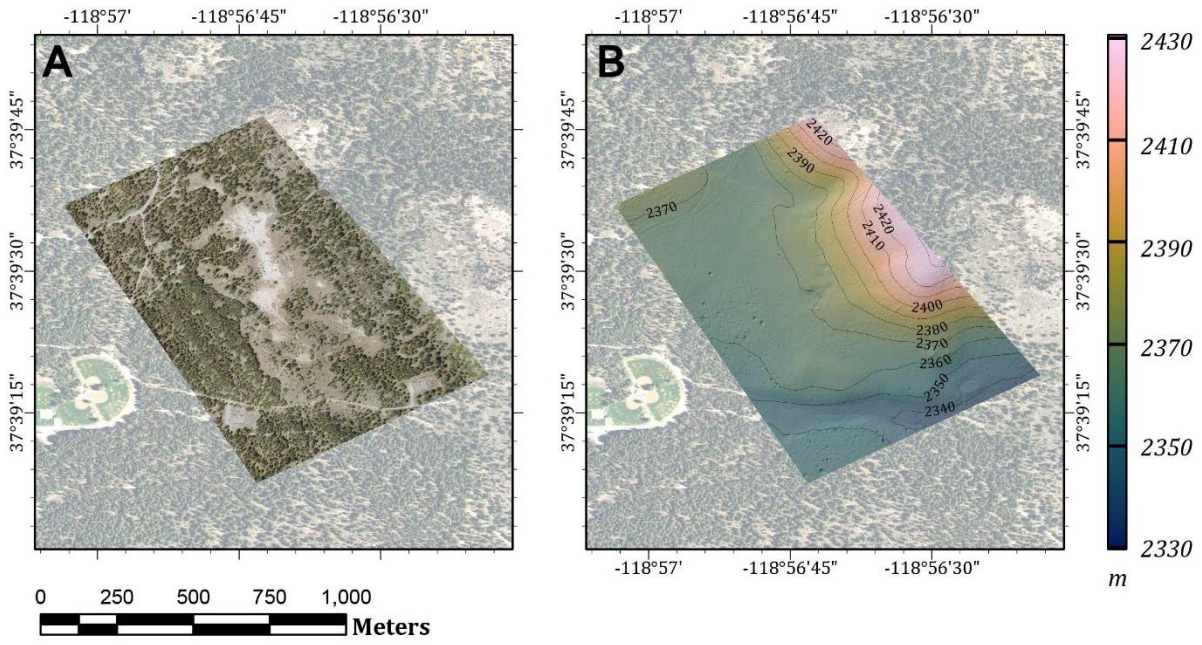

Figure 4: Results of the SfM survey. (A) 5 cm/pixel orthomosaic, embedded in semitransparent NAIP imagery. (B) 20 cm/pixel DEM, shown with 10 m contours.

We also measured diurnal variations of Earth's magnetic field using a Geometrics G856 magnetometer base station at a fixed location for both field sessions (blue box in Figure 1B). We used these data to correct the UAS magnetic data for temporal variations and to determine a scalar value (48,000 nT) to convert the MagDrone vector data to absolute values. In addition, each magnetic survey day began with a calibration flight, consisting of an eight-leaf clover pattern at 7 m/s and 120 m constant elevation, over a site in the study area with relatively low magnetic gradient (blue star in Figure 1B). These calibration flights were used in post-processing to evaluate magnetic perturbations of the UAS and compensate for unwanted magnetic signals from the aircraft, using the software of Kaub et al. (2021), based on the method of Munschy et al. (2007).

We removed all turns and corners from the magnetic surveys to enhance data quality. There was a notable difference between the surveys flown in May and October 2021. This offset was not fully corrected by the base station data, but it is expected when merging multiple magnetic surveys that were recorded with a vector magnetometer and converted to absolute values using an estimated scalar value. Kaub et al. (2021) compared overlapping surveys by subtracting the mean of the area of overlap. A similar method was performed here, resulting in a calculated average difference between the May and October surveys of -70 nT, which was used to merge the two datasets; however, the overlap between the surveys was smaller than ideal for constraining the estimated offset. Therefore, some artefacts may remain at the margin between the two grids. We then levelled the data, by correcting for errors at intersections with tie lines that follow a trend. A fourth order trend was selected as the best fit for the data, and the resulting magnetic data were gridded (Figure 5A).

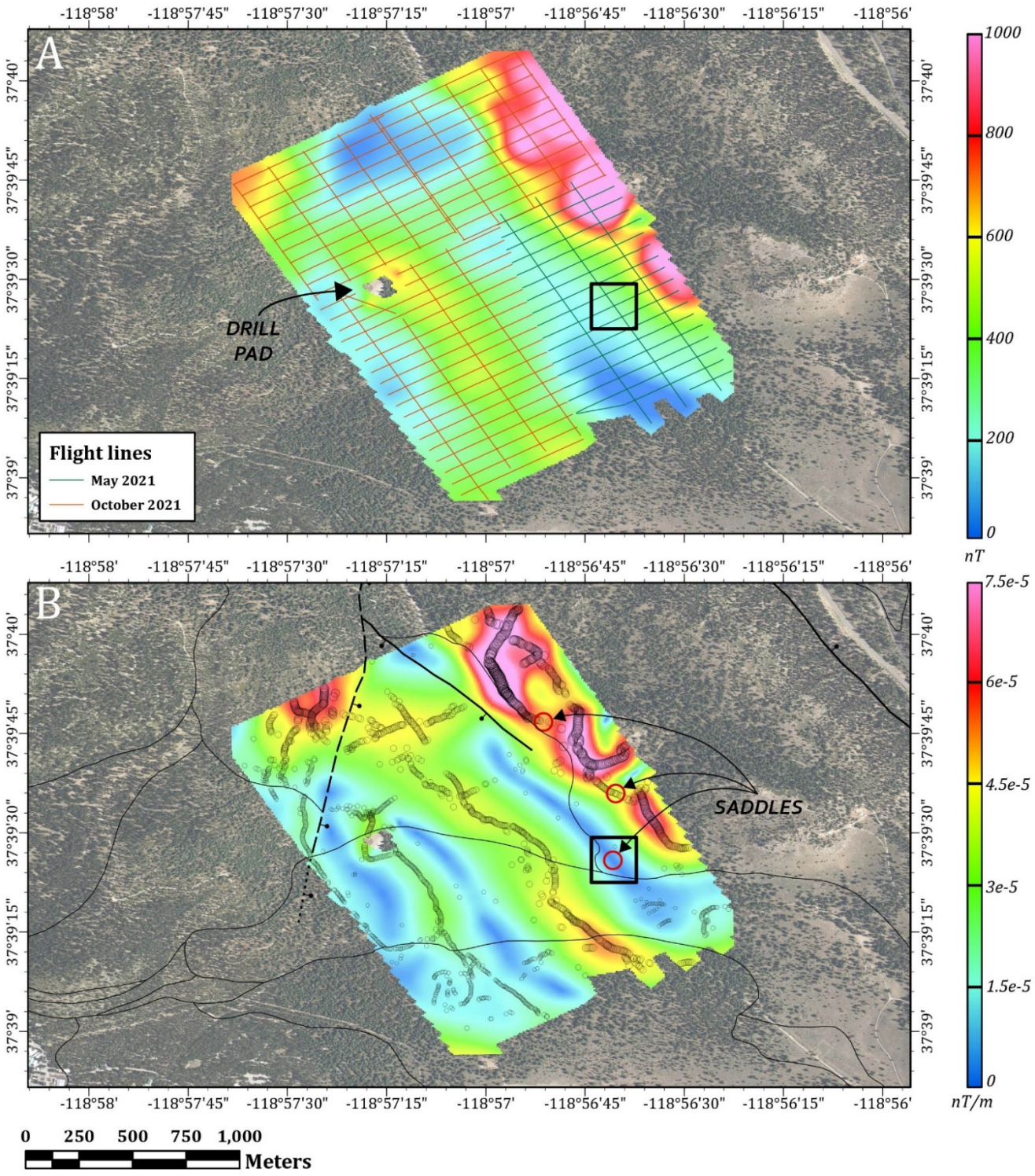

Figure 5: (A) Magnetic anomaly map from UAS survey, with flight line locations. (B) Horizontal gradient of the pseudogravity grid, with ridges shown as open circles sized to the gradient magnitude, and selected saddles of potential interest shown as red circles. Black lines show contacts and normal faults from the geologic map (Figure 2). Black boxes indicate the extent of the thermal area shown in Figure 7A,B. Imagery acquired by the U.S. Department of Agriculture as part of NAIP.

For aiding interpretation of buried structures, we also transformed the magnetic anomaly to pseudogravity, which converts the anomaly into what would be observed if the magnetic distribution of the body were replaced by an identical density distribution (Baranov, 1957). We calculated the horizontal gradient (HG) magnitude of the pseudogravity, which identifies steep or near-vertical lateral changes in magnetization and therefore assists with mapping subsurface geology (Blakely and Simpson, 1986). We classified the gradient extrema according to the method of Phillips et al. (2007), paying particular attention to the ridges and saddles (Figure 5B).

The magnetic maps (Figure 5) are very high-resolution due to the relatively low flight height of 60 m, which would be impossible in a fixed-wing occupied aircraft and unsafe in a helicopter, given the height of trees in the area. The maps show prominent NW-SE trends, with the HG map revealing several smaller potential saddle features, which may be associated with fault intersections. The extrema toward the eastern edge of the survey area appear to coincide with the contact between the rhyolitic and glacial units. The other features observed in these maps are likely to represent faults or other structures that could be important controls on the hydrothermal system. Numerous HG saddles are concentrated around the central thermal anomaly (boxed area in Figure 5B). The thermal and gas anomalies are located primarily along an HG low, which could indicate hydrothermal alteration, and extend approximately parallel to the gradient, toward the apparent saddle visible near the eastern edge of both maps. This saddle may represent the intersection of a continuation of the mapped fault with an additional, unmapped structure. Further work will be needed to investigate these features in the magnetic surveys, to determine whether they play an important role in controlling the hydrothermal surface expressions.

The hole in the data in the western half of the study area spanned an active drill pad; we modified the UAS flight path due to the presence of a drill rig taller than our 60 m flight height. The magnetic high just to the east of this gap is likely associated with the drilling infrastructure and other cultural features in this area. After the drill rig has left, an additional magnetic survey could include filling this gap, although some cultural features may remain.

4. Thermal Infrared Imagery

Thermal infrared images were collected with a FLIR Duo Pro R camera mounted on a Gremsy S1 V3 gimbal fixed under the DJI Matrice 600 Pro (Figure 3C). Images were captured at 1 Hz, with a flight speed of 4 m/s at a height of 120 m, with 90% side and forward overlap, for a ground resolution of 14 cm, with flight lines oriented NNW-SSE. The radiometric parameters were set to an emissivity of 0.96 and an air temperature of 7 °C, with medium humidity, and data were collected at night, between 8 and 11 pm, to minimize the effect of solar irradiance. To geospatially correct the imagery, three thermal blankets were laid on the ground and their locations measured with a Trimble Geo7X differential GPS, which has a post-processing vertical and horizontal precision of <5 cm. The images were processed in Agisoft Metashape. Due to issues with the sensor's calibration drift, we used the built-in color calibration tool in Metashape to correct erroneously bright or dark images prior to generating a 13 cm/pixel thermal orthomosaic. Raw digital numbers (DN) were converted to temperature using the equation

$$T = DN * 0.04 - 273.15,$$

where T is in degrees Celsius (FLIR, 2017).

The TIR orthomosaic displays a prominent thermal high in the center of the tree kill area, consistent with observations of hydrothermal surface features (Figure 6). The thermal contrast between the main thermal area (box labeled "A,B" in Figure 6) and the surrounding area is distinct, and several other possible hot spots are visible in the eastern and southern areas of the orthomosaic (e.g., circled area in Figure 6). The roads and vegetation also appear as relatively warm features.

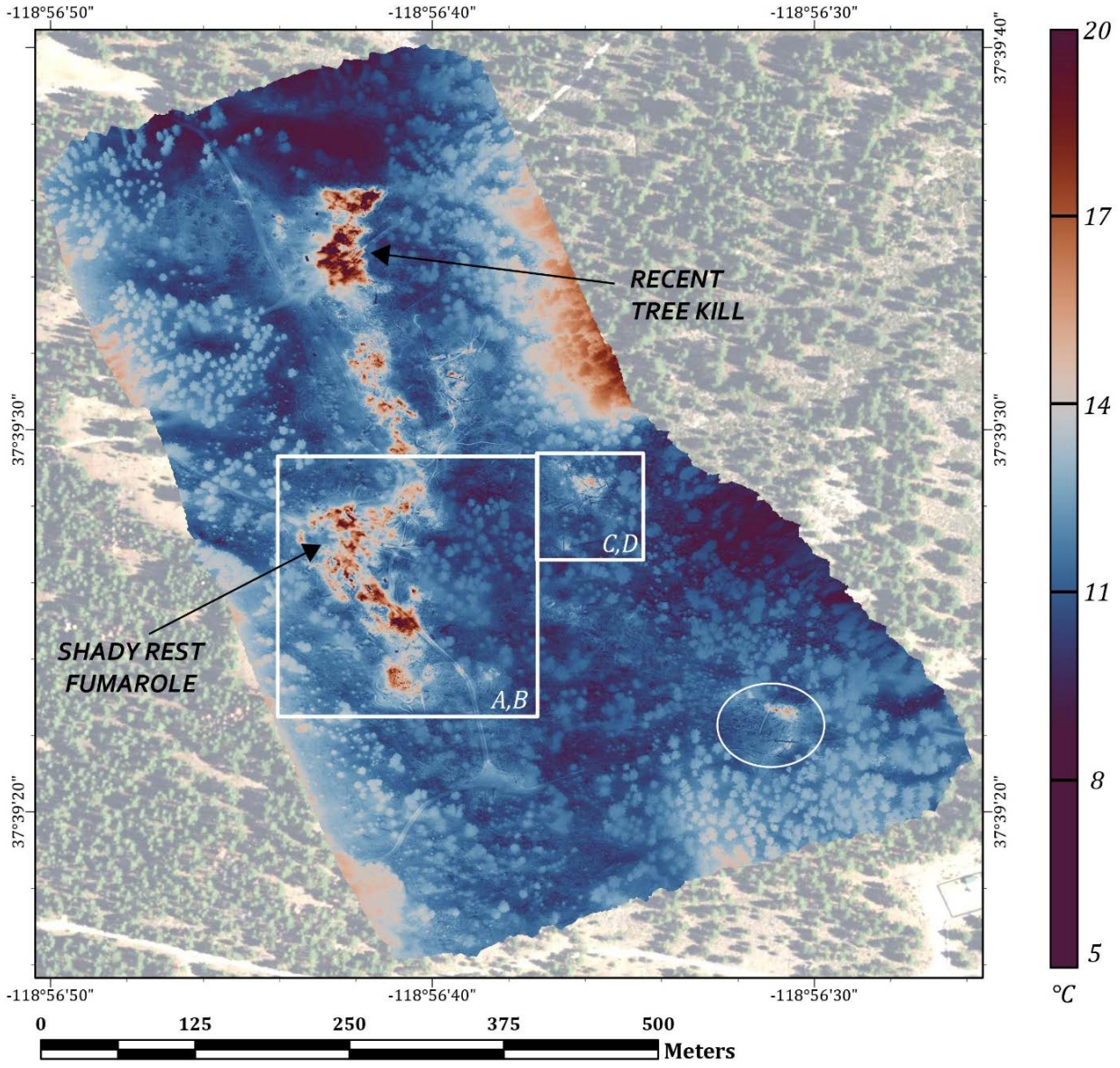

Figure 6: TIR orthomosaic of the central tree kill area of Shady Rest, after color calibration and conversion to temperature values. White boxes indicate extents of detailed areas shown in Figure 7. Selected surface expressions of hydrothermal activity are from Bergfeld and Evans (2011). Circled hot spot indicates thermal anomaly outside of main thermal area that appears to coincide with a secondary tree kill area.

At the beginning of the October 2021 field session, we discovered that our thermal camera (FLIR Duo Pro R) was experiencing calibration issues beyond the range of the calibration drift typical of uncooled thermal cameras. Kelly et al. (2019) found that a FLIR Vue Pro (using a sensor very similar to that of the Duo Pro R) experienced ± 5 ° temperature variations as a result of wind and changes in ambient temperature throughout the course of an average UAS flight. In addition to this calibration drift, we determined that the camera was performing faulty non-uniformity corrections (NUC) every ~1-4 minutes, resulting in significant jumps (≥5 °C) up or down in recorded temperature values. The resulting orthomosaic was characterized by flight-line-parallel trends. While Metashape's color calibration tool removed the bulk of the erroneous features, particularly in the central areas with higher overlap, the numerical accuracy of the resulting values is to be treated with caution. Furthermore, edge effects remain, especially apparent in the temperature high along the eastern edge of the orthomosaic, likely a vestige of the camera's calibration drift.

Comparison between the TIR orthomosaic from this study and that from Vaughan et al. (2018) yields compellingly similar results (Figure 7). Both surveys define the same shape for the central thermal area (Figure 7A,B) with the UAS-borne TIR orthomosaic showing the anomaly at considerably higher resolution (13 cm vs. 90 cm). The new TIR survey also provides confirmation of several smaller thermal anomalies on the outskirts of the main anomaly, as in Figure 7C-D, which corresponds with a pronounced tree kill area. The high resolution of the UAS-borne orthomosaic shows evidence of even smaller anomalies not observable in the previous survey in the south and east of Figure 7D (circled features).

Although the two surveys show strong correspondence in relative values, the two differ significantly in absolute temperature values, with the UAS-borne survey being ~10 ° warmer than the occupied aircraft survey. Part of this discrepancy likely stems from natural variations, because the surveys were collected five years apart, and the occupied aircraft survey was flown later at night, when it was likely to be colder and the effects of solar irradiance smaller. Both surveys, however, were flown in mid-October, and operators recorded similar ambient temperatures. The discrepancy could therefore also be a result of variations in calibration methods and corrections, particularly given that two different sensors were used (FLIR Duo Pro R vs. FLIR SC6000), with different wavelength ranges and pixel sizes, and at considerably different flight heights (120 vs. 1,800 m).

While UAS-borne TIR imagery is still a burgeoning field, the potential for further applications of high-resolution TIR methods to hydrothermal systems is encouraging. Even with a faulty sensor, the detail with which the camera can discern thermal areas promises ample applications for mapping and monitoring hydrothermal systems. Currently, the technology is limited by the relatively low resolution of thermal sensors, compared to visible wavelength sensors, which when coupled with the single-band nature of TIR, necessitates more demanding surveys. Overlap and sidelap for TIR surveys are often around the ~90% values used in this study, meaning that flights take considerably longer than their visible counterparts. Nonetheless, these results suggest that the additional effort required for TIR surveys is warranted.

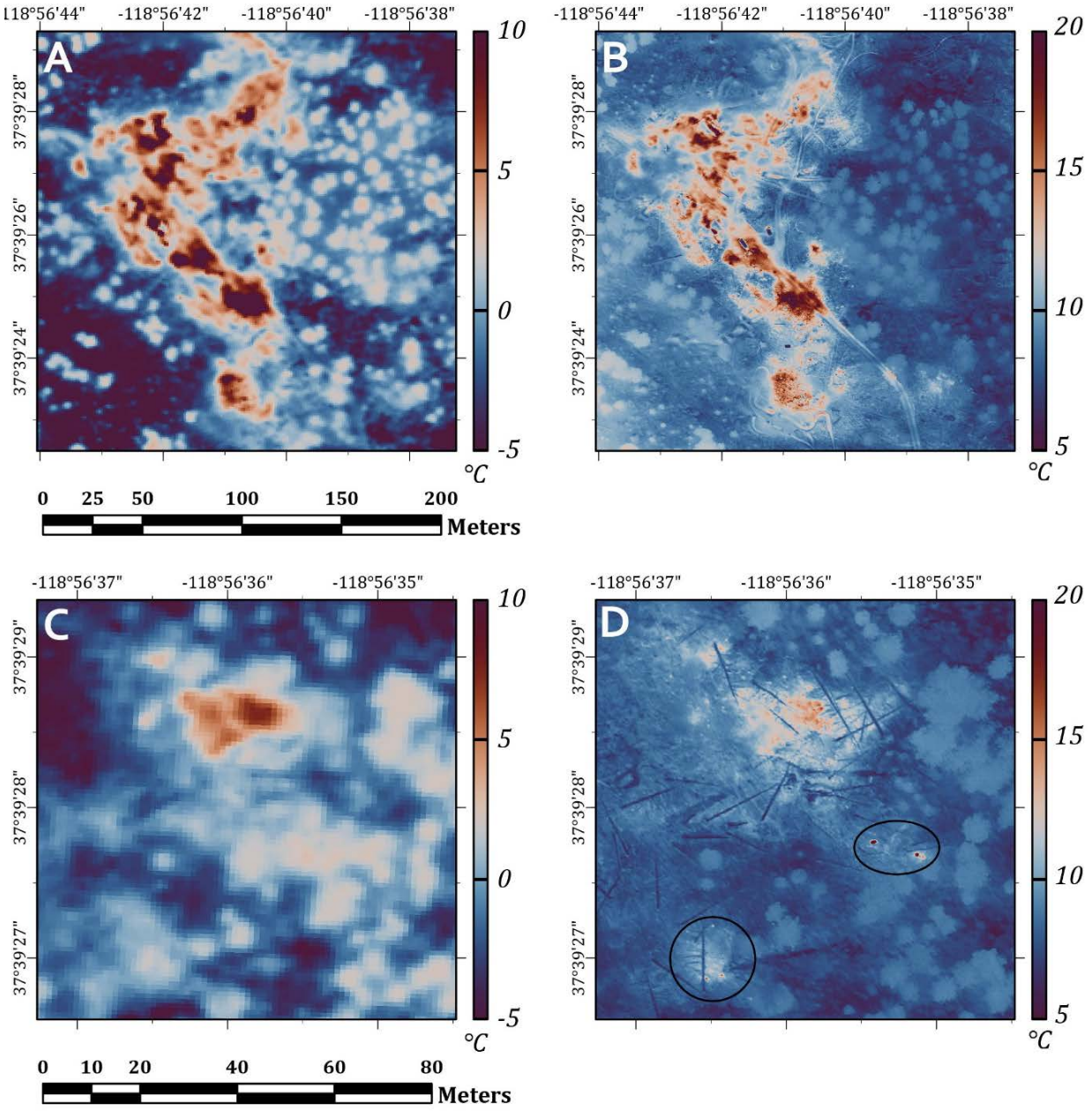

Figure 7: Detailed views of the TIR orthomosaic. (A) and (C) show the commercial TIR survey flown by Vaughan et al. (2018). (B) and (D) show corresponding views of the TIR survey flown in this study. Many of the features visible are vegetation, including living shrubs and trees (warmer circular features) and fallen trees (colder linear features). Note difference in temperature scale between AC and BD. Circled areas in D indicate thermal anomalies not captured by the resolution of the occupied aircraft survey.

5. Multi-GAS

Gas measurements were performed using a U.S. Geological Survey UAS Multi-GAS instrument mounted below the DJI Matrice 600 Pro (Figure 3D). This instrument measures four gases: carbon dioxide (CO_2), sulfur dioxide (SO_2), hydrogen sulfide (H_2S), and water vapor (H_2O). Gas data collection focused on the tree kill and gas vent area at Shady Rest, as well as a drill pad to the northwest, at which we established a baseline for UAS-borne measurements before the drilling began. We planned flights with several different flight heights and speeds in order to determine acceptable parameters for gas data acquisition (Figure 8). Configurations included: 5 m at 1 m/s; 10 m at 3 m/s; 15 m at 2 m/s; 20 m at 3 m/s; 30 m at 2 and 3 m/s; and 50 m at 5 m/s.

The data require additional processing before they can be interpreted. However, general lessons about the application of UAS-based gas measurements may still be gleaned. Implementation of the UAS Multi-GAS system in monitoring hydrothermal systems is complex, since gas concentrations at the survey heights may be below the resolution of the instrument. Employing the Multi-GAS instrument requires a balance between maintaining a low enough flight height to measure a detectable signal and flying high enough to avoid trees and other potential obstacles. Flying at 30 m or lower is impractical across much of the study area (outside of the tree kill) due to the thick tree cover.

Additional challenges may arise under windy conditions that may diffuse gas concentrations. With further development of these applications in consideration of these challenges, we anticipate that UAS-based gas measurements will prove a valuable tool for mapping and monitoring hydrothermal systems, especially when used in conjunction with other methods.

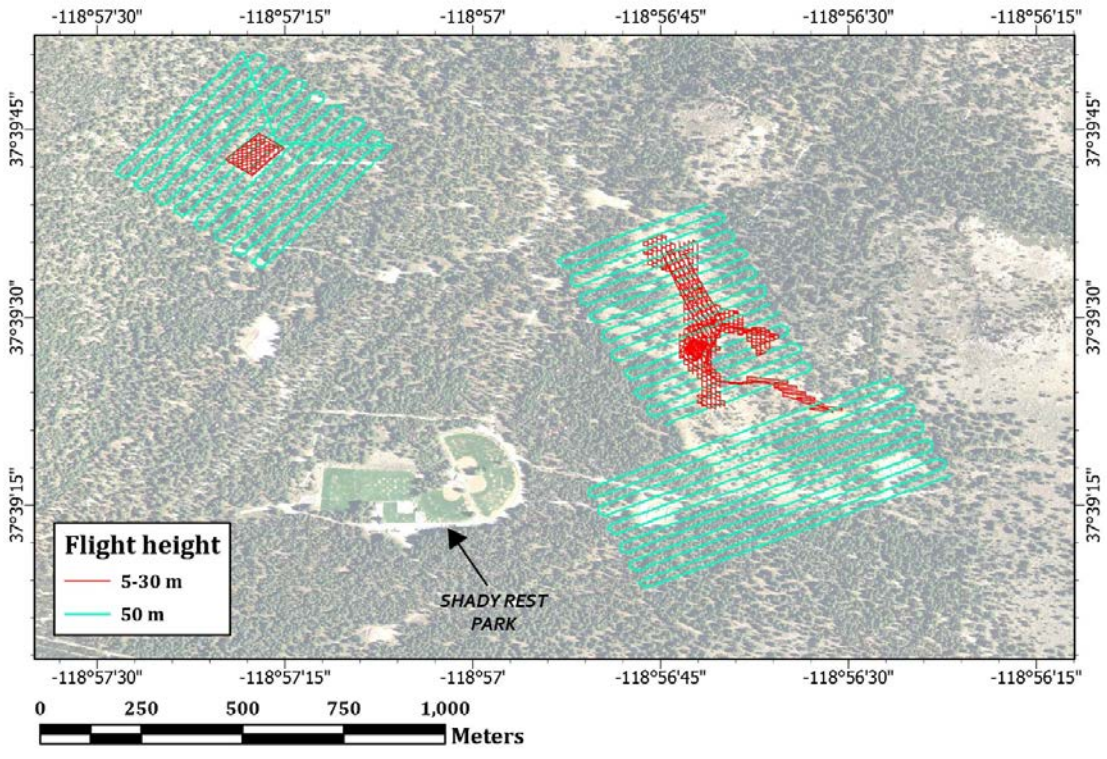

Figure 8: Orthomosaic showing flight lines from UAS gas surveys, including larger-scale surveys flown at a height of 50 m and more detailed surveys flown at heights of 5, 10, 15, 20, or 30 m.

6. Gravity

In addition to the UAS-borne measurements, 73 new ground-based gravity stations were acquired to fill in gaps in the existing gravity dataset and aid in subsurface interpretation. Data were collected with a Scintrex CG-5 gravimeter and tied daily to a new base station established as part of this study. The new base station, FSVC2 (37.64785°, -118.96049°; observed gravity: 979,232.602 mGal), is located at the Mammoth Lakes Welcome Center, managed by the U.S. Forest Service (black square in Figure 1B). It is an outdoor alternative to the nearby indoor absolute base station FSVC (37.64776°, -118.96027°; observed gravity: 979,232.518 mGal), to which it was tied with a quadruple-loop base tie. Location and elevation data for stations were collected with a Trimble Geo 7X differential GPS, which has a post-processing vertical and horizontal precision of <5 cm.

The gravity data were processed following the methods outlined by Blakely (1995), using a suite of in-house software that apply several corrections, including tide, instrument drift, latitude, free-air, Bouguer, curvature, terrain within 167 km, and isostatic compensation of topography. The reduction density used was 2.67 g/cm^3. Existing gravity data in the study area from the public domain PACES database (Hildenbrand et al., 2002) were also re-reduced using these methods and merged with the new data.

The isostatic anomaly map produced from the gravity data (Figure 9) shows that most of the new data were collected in a gravity low near the southwestern edge of the large gravity low that characterizes the Long Valley Caldera. The new data help to further constrain the gradient at the southern edge of the caldera and fill in a major gap in the existing data.

A residual gravity grid was generated by upward continuing the isostatic anomaly grid to 1 km and subtracting this from the original grid (Figure 10A). As with the magnetic data, we calculated the horizontal gradient magnitude of the isostatic anomaly, which identifies steep or near-vertical lateral changes in density and therefore assists with mapping subsurface geology (Blakely and Simpson, 1986; Figure 10B). These derivative products highlight potential structures, some of which show general correspondence with the faults mapped by Robinson et al. (2016), but with the suggestion of additional potential controlling structures in the central thermal area.

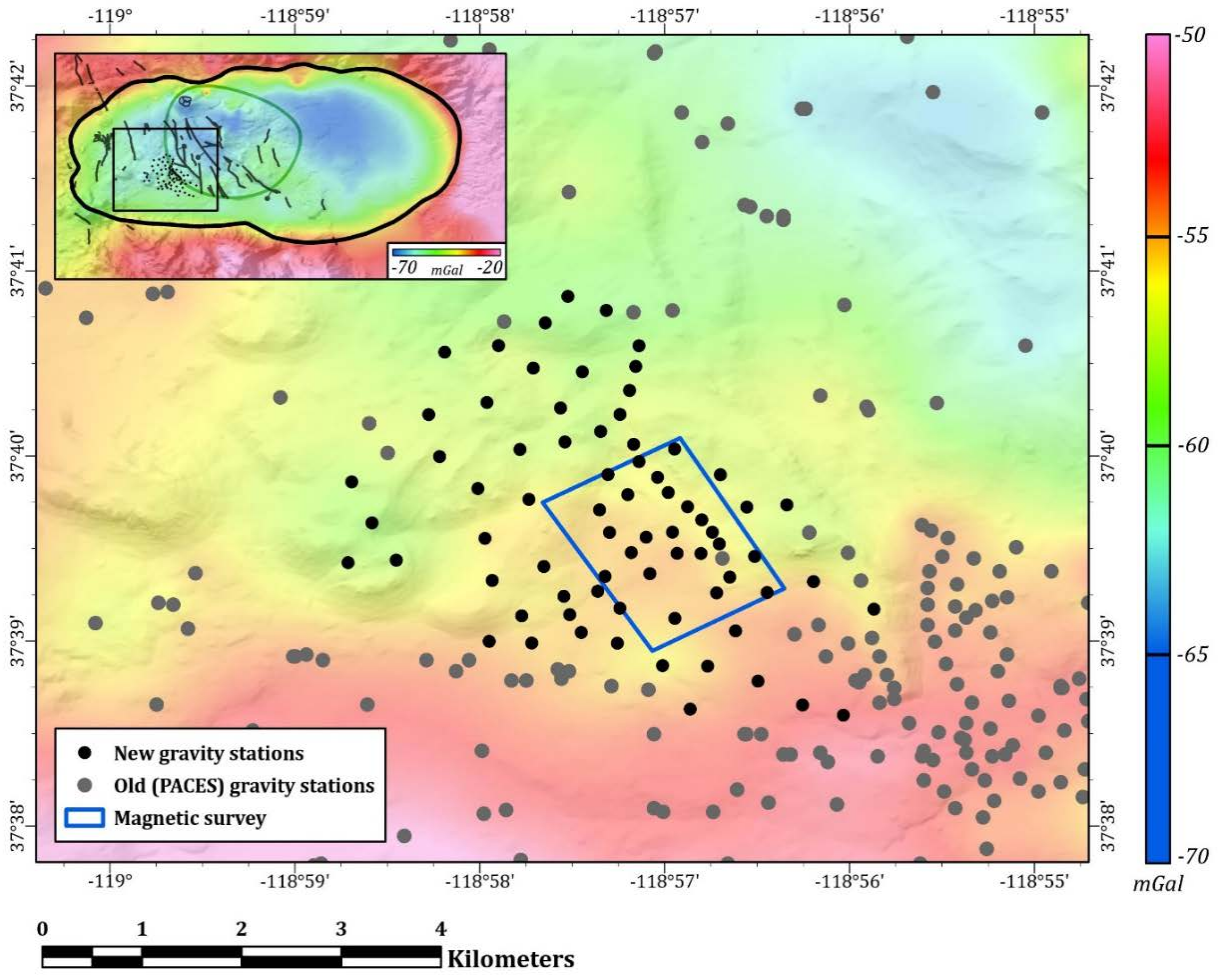

Figure 9: Isostatic anomaly map produced from merging the new and existing gravity data. Inset shows regional isostatic anomaly with new gravity data shown as black dots (different color scale). Green line is resurgent dome.

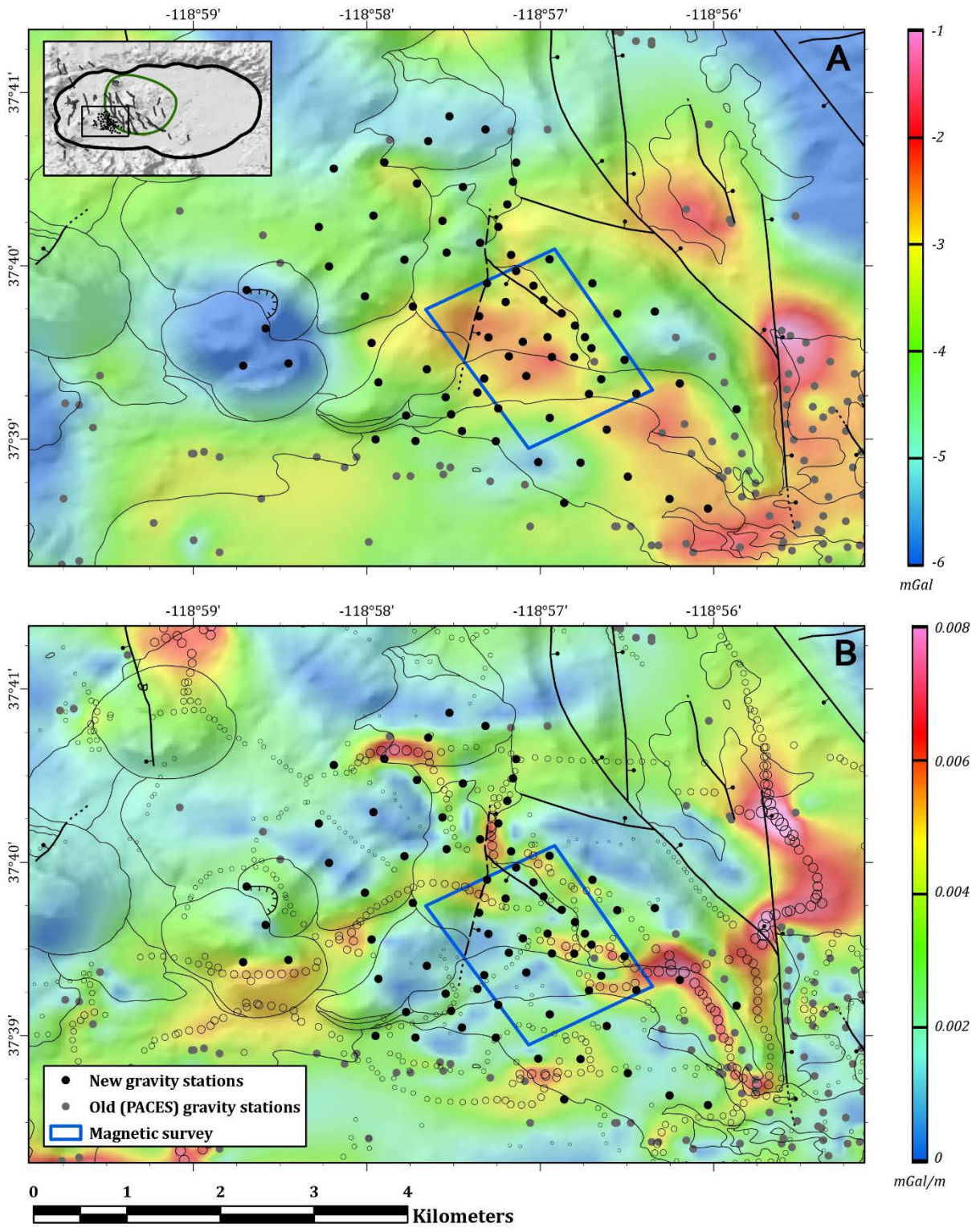

Figure 10: Derivative gravity maps, with geologic contacts and normal faults from Robinson et al. (2016). Solid black and gray circles show gravity measurements. (A) Residual gravity map, produced by subtracting a regional field created by 1 km upward continuation of the isostatic anomaly grid. (B) Horizontal gradient of the isostatic gravity, with gradient maxima (ridges) shown as open circles sized to the gradient magnitude. See Figure 2 for more detailed geologic map.

Extrema derived from the gravity data appear to correspond with those in the northern portion of the magnetic survey, particularly just west of the northernmost of the potential saddle features indicated in Figure 5B. This correlation may indicate that an unmapped structure, possibly associated with the saddle, extends E-W across the northern portion of the magnetic survey. However, the more regional scale of the gravity data, in comparison with the magnetic, thermal, and gas data, makes it somewhat difficult to correlate features across datasets. Additional data acquisition along detailed profiles would help resolve this limitation.

7. Conclusions

In this study, we collected complementary datasets of structure from motion, magnetic, thermal infrared, gas, and gravity measurements at the thermal area of Shady Rest in Mammoth Lakes, California, as part of an ongoing effort to better understand the subsurface features controlling the hydrothermal system and to monitor potential changes. The goal of this study was to assess the utility of these methods for mapping and monitoring hydrothermal systems and to determine best practices for their application.

While we have substantial coverage, future work with UAS tools in the Mammoth Lakes area could enhance our understanding of the hydrothermal system. This work might focus on collecting additional TIR data in the Shady Rest area, particularly with a thermal camera less prone to calibration drift. It may be beneficial to fly additional magnetic tie lines, for levelling purposes, and to extend the magnetic survey farther east, to investigate the magnetic features observed along the eastern margin of the existing survey. In addition, a similar dataset may be acquired at nearby Horseshoe Lake (Figure 1A), another site with extensive tree kill, where we have already collected SfM data. Future work may also involve integrating existing hiked magnetic and gas surveys and soil gas measurements, with a focus on investigating controls on the hydrothermal system.

Whereas UAS-borne magnetometry, SfM, and gravity measurements are all well-established methods in the geosciences, UAS-borne gas and TIR methods are still emerging fields that require additional work to determine best practices. Although all UAS-based tools are inherently weather-dependent, as it is unsafe to fly in strong winds or precipitation, both the TIR and Multi-GAS sensors are especially dependent on – and influenced by – changes in ambient conditions. With the thermal sensor, it is best to fly at night, when solar irradiance is minimal, and to include significant overlap (~90%) between flight lines, both of which can make surveys demanding for field crews. The radiometric calibration of the thermal camera also depends greatly on the ambient conditions of the survey, particularly the temperature, which in turn depends on the wind conditions at altitude and is very difficult to account for. After further developments in methods and processing steps, the TIR and Multi-GAS sensors will likely join magnetics, gravity, and SfM as invaluable tools in the mapping and monitoring of hydrothermal systems. However, our results demonstrate that these tools can still be informative in their current design, particularly when used in conjunction with the other sensors examined in this study.

Acknowledgements

We are grateful to Claire Bouligand and Leon Kaub for their assistance with the magnetic data reduction, and to Stuart Wilkinson and John Minnick for their help in the field. We also thank

Vicki Langenheim and Michelle Roberts for their feedback, which greatly improved the manuscript. At the time of this study William Schermerhorn was a Physical Science Technician with the U.S. Geological Survey. This work was funded by the Geothermal Resources Investigations Project (GRIP), with support from the U.S. Geological Survey's Energy Program. Any use of trade, firm, or product names is for descriptive purposes only and does not imply endorsement by the U.S. Government.

REFERENCES

Bailey, R.A. "Geologic Map of Long Valley Caldera, Mono-Inyo Craters Volcanic Chain, and Vicinity, Mono County, California." *U.S. Geological Survey Miscellaneous Investigations Map I-1933*, scale 1:62,500, (1989).

Bailey, R.A., Dalrymple, G.B., and Lanphere, M.A. "Volcanism, Structure, and Geochronology of Long Valley Caldera, Mono County, California." *Journal of Geophysical Research,* 81, no. 5, (1976), 725-744.

Baranov, V. "A New Method for Interpretation of Aeromagnetic Maps: Pseudo-gravimetric Anomalies." *Geophysics*, 22, no. 2, (1957), 359-382.

Bergfeld, D., and Evans, W.C. "Monitoring CO2 Emissions in Tree-kill Areas Near the Resurgent Dome at Long Valley Caldera, California." *USGS Scientific Investigations Report*, 2011-5038, (2011).

Bergfeld, D., Vaughan, R.G., Evans, W.C., and Olsen, E. "Monitoring Ground-Surface Heating During Expansion of the Casa Diablo Production Well Field at Mammoth Lakes, California." *Geothermal Resources Council Transactions*, 39, (2015), 1007-1013.

Blakely, R.J. "Potential theory in gravity and magnetic applications." Cambridge University Press, New York, (1995), 441 p.

Blakely, R.J., and Simpson, R.W. "Approximating Edges of Source Bodies from Gravity or Magnetic Data." *Geophysics*, 51, (1986), 1494–1498.

Chesley, J. T., Leier, A.L., White, S., and Torres, R. "Using Unmanned Aerial Vehicles and Structure-from-Motion Photogrammetry to Characterize Sedimentary Outcrops: An example from the Morrison Formation, Utah, USA." *Sedimentary Geology,* 354, (2017), 8 p.

Chio, S.H., and Lin, C.H. "Preliminary Study of UAS Equipped with Thermal Camera for Volcanic Geothermal Monitoring in Taiwan." *Sensors*, 17, no. 7, (2017), 17 p.

De Smet, T.S., Nikulin, A., Romanzo, N., Graber, N., Dietrich, C., and Puliaiev, A. "Successful Application of Drone-based Aeromagnetic Surveys to Locate Legacy Oil and Gas Wells in Cattaraugus County, New York." *Journal of Applied Geophysics*, 186, (2021), 12 p.

FLIR, "Duo Pro R User Guide, Rev. 1.0." (2017), 50 p.

Harvey, M.C., Rowland, J.V., and Luketina, K.M. "Drone with Thermal Infrared Camera Provides High Resolution Georeferenced Imagery of the Waikite Geothermal Area, New Zealand." *Journal of Volcanology and Geothermal Research*, 325, (2016), 61-69.

Hildreth, W., and Fierstein, J. “Eruptive History of Mammoth Mountain and Its Mafic Periphery, California.” *U.S. Geological Survey Professional Paper*, 1812, (2016), 128 p., 2 plates, scale 1:24,000.

Hildenbrand, T.G., Briesacher, A., Flanagan, G., Hinze, W.J., Hittelman, A.M., Keller, G.R., Kucks, R.P., Plouff, D., Roest, W., Seeley, J., Smith, D.A., and Webring, M. “Rationale and Operational Plan to Upgrade the U.S. Gravity Database.” *U.S. Geological Survey Open-File Report 02-463*, (2002), 12 p. [Data downloaded in October 2007 from URL http://paces.geo.utep.edu/research/gravmag/gravmag.shtml]

Jackisch, R., Lorenz, S., Kirsch, M., Zimmermann, R., Tusa, L., Pirttijärvi, M., Saartenoja, A., Ugalde, H., Madriz, Y., Savolainen, M., and Gloaguen, R. “Integrated Geological and Geophysical Mapping of a Carbonatite-hosting Outcrop in Siilinjärvi, Finland, using Unmanned Aerial Systems.” *Remote Sensing*, 12, no. 18, (2020), 31 p.

Kaub, L., Glen, J.M.G., Bouligand, C., Lamb, A.P., Ritzinger, B., Teodorescu, M., Hurley, K., Ham, R., and Williamson, M. “Developing Small Unmanned Aerial Systems (sUAS) for High-Resolution Aeromagnetic Mapping Applications in the Geosciences.” *Proceedings World Geothermal Congress*, (2020), 9 p.

Kaub, L., Keller, G., Bouligand, C., and Glen, J.M.G. “Magnetic Surveys with Unmanned Aerial Systems: Software for Assessing and Comparing the Accuracy of Different Sensor Systems, Suspension Designs and Compensation Methods.” *Geochemistry, Geophysics, Geosystems*, 22, (2021), 19 p.

Kelly, J., Kljun, N., Olsson, P.O., Mihai, L., Liljeblad, B., Weslien, P., Klemedtsson, L., and Eklundh, L. “Challenges and Best Practices for Deriving Temperature Data from an Uncalibrated UAV Thermal Infrared Camera.” *Remote Sensing*, 11, no. 5, (2019), 21 p.

Lewicki, J.L. “Long-term Year-round Observations of Magmatic CO_2 Emissions on Mammoth Mountain, California, USA.” *Journal of Volcanology and Geothermal Research*, 418, (2021), 13 p.

Liu, E.J., Wood, K., Mason, E., Edmonds, M., Aiuppa, A., Giudice, G., Bitetto, M., Francofonte, V., Burrow, S., Richardson, T., Watson, M., Pering, T.D., Wilkes, T.C., McGonigle, A.J.S., Velasquez, G., Melgarejo, C., and Bucarey, C. “Dynamics of Outgassing and Plume Transport Revealed by Proximal Unmanned Aerial System (UAS) Measurements at Volcán Villarrica, Chile.” *Geochemistry, Geophysics, Geosystems*, 20, no. 2, (2019), 730-750.

Müller, D., Bredemeyer, S., Zorn, E., De Paolo, E., and Walter, T.R. “Surveying Fumarole Sites and Hydrothermal Alteration by Unoccupied Aircraft Systems (UAS) at the La Fossa Cone, Vulcano Island (Italy).” *Journal of Volcanology and Geothermal Research*, 413, (2021), 18 p.

Munschy, M., Boulanger, D., Ulrich, P., and Bouiflane, M. “Magnetic Mapping for the Detection and Characterization of UXO: Use of Multi-sensor Fluxgate 3-axis Magnetometers and Methods of Interpretation.” *Journal of Applied Geophysics*, 61, no. 3-4, (2007), 168-183.

Nishar, A., Richards, S., Breen, D., Robertson, J., and Breen, B. “Thermal Infrared Imaging of Geothermal Environments and by an Unmanned Aerial Vehicle (UAV): A Case Study of the Wairakei–Tauhara Geothermal Field, Taupo, New Zealand.” *Renewable Energy*, 86, (2016), 1256-1264.

Parvar, K., Braun, A., Layton-Matthews, D., and Burns, M. “UAV Magnetometry for Chromite Exploration in the Samail Ophiolite Sequence, Oman.” *Journal of Unmanned Aerial Systems*, 6, no. 1, (2017), 57-69.

Phillips, J.D., Hansen, R.O., and Blakely, R.J. “The Use of Curvature in Potential-field Interpretation.” *Exploration Geophysics*, 38, (2007), 111-119.

Präg, M., Becker, I., Hilgers, C., Walter, T.R., and Kühn, M. “Thermal UAS Survey of Reactivated Hot Spring Activity in Waiwera, New Zealand.” *Advances in Geosciences*, 54, (2020), 165-171.

Robinson, J.E., Hildreth, W., and Fierstein, J. “Database for the Eruptive History of Mammoth Mountain and Its Mafic Periphery, California.” *U.S. Geological Survey Professional Paper*, 1812, (2016).

Sorey, M.L., Evans, W.C., Kennedy, B.M., Farrar, C.D., Hainsworth, L.J., and Hausback, B. “Carbon Dioxide and Helium Emissions from a Reservoir of Magmatic Gas beneath Mammoth Mountain, California.” *Journal of Geophysical Research: Solid Earth*, 103, no. B7, (1998), 15303-15323.

Sorey, M.L., Farrar, C.D., Marshall, G.A., and Howie, J.F. “Effects of Geothermal Development on Deformation in the Long Valley Caldera, Eastern California, 1985–1994.” *Journal of Geophysical Research: Solid Earth,* 100, no. B7, (1995), 12475-12486.

Stix, J., de Moor, J.M., Rüdiger, J., Alan, A., Corrales, E., D'Arcy, F., Diaz, J.A., and Liotta, M. “Using Drones and Miniaturized Instrumentation to Study Degassing at Turrialba and Masaya Volcanoes, Central America.” *Journal of Geophysical Research: Solid Earth*, 123, no. 8, (2018), 6501-6520.

Vaughan, R.G., Bergfeld, D., Evans, W.C., Wilkinson, S., Miwa, C., and Diabat, M. “A Baseline Thermal Infrared Survey of Ground Heating around the Casa Diablo Geothermal Plant, Mammoth Lakes, CA.” *Geothermal Resources Council Transactions*, 42, (2018).

Walter, C., Braun, A., and Fotopoulos, G. “High-resolution Unmanned Aerial Vehicle Aeromagnetic Surveys for Mineral Exploration Targets.” *Geophysical Prospecting*, 68, (2020), 334-349.